Thin–Walled Structures 203 (2024) 112222

Contents lists available at ScienceDirect

Thin-Walled Structures

journal homepage: www.elsevier.com/locate/tws

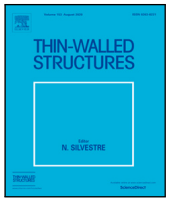

# Quantifying efficient shape-shifting: Energy barrier measurement in multi-stable lattice metamaterials

Qicheng Zhang [a,1], Jiajia Shen [a,b,*,1], Martin Garrad [c,d], Fabrizio Scarpa [a], Alberto Pirrera [a], Rainer M.J. Groh [a]

[a] Bristol Composites Institute (BCI), School of Civil, Aerospace and Design Engineering, University of Bristol, Bristol BS8 1TR, UK
[b] Exeter Technologies Group (ETG), Department of Engineering, University of Exeter, Exeter EX4 4QF, UK
[c] Department of Engineering Mathematics, University of Bristol, Bristol BS8 1TW, UK
[d] SoftLab, Bristol Robotics Laboratory, University of Bristol and University of the West of England, Bristol BS16 1QY, UK

## ARTICLE INFO

Dataset link: https://data.bris.ac.uk/data/dataset/1n7g692ynrlht214cxm7yk77qi

*Keywords:*
Snap-through instability
Multi-axial testing
Embedded actuation
Well-behaved nonlinear structures
Structural testing
Energy barrier

## ABSTRACT

Shape-shifting between multiple stable deformation states offers attractive pathways to design adaptive structures. Ideas have been conceptualised in diverse fields, including soft robotics and aerospace engineering. The success of shape-shifting relies on overcoming the energy barrier separating adjacent stable configurations, which necessitates efficient actuation strategies. Recently, multistable mechanical metamaterials have been designed with shape-shifting controlled by an actuator at the local scale, *i.e* with embedded actuation. This local, embedded actuation creates challenges for quantifying the energy barriers required for shape-shifting. Specifically, the local actuation requires a pair of forces with opposite directions and the direction of the forces must remain constant throughout the entire loading process. Moreover, the loading points must move freely in a direction perpendicular to the loading direction. We present a novel bi-axial test rig for a typical multi-stable lattice metamaterial that accurately determines the energy barrier between stable states by using an embedded actuator and inducing shape-shifting. Our experimental design features two independent actuation systems operating at different length scales: a primary one for a globally applied axial compression of the metamaterial, and a secondary local system for triggering shape-shifting between different stable configurations. Experimental data obtained using this bespoke test rig unveil the metamaterial's response to local, embedded actuation. Excellent agreement with finite element simulations is observed, demonstrating the effectiveness of the test setup in providing measurements of the energy barrier. This work provides a valuable benchmark for measuring energy barriers in multi-stable metamaterials and paves the way for rigorous validation and verification of novel functional metamaterial and structures that leverage shape-shifting mechanisms.

## 1. Introduction

Structural instabilities, traditionally treated as failure modes in engineering design [1–3], are increasingly being exploited for functionality [4,5]. Their applications include (but are not limited to) hinge-less shape-shifting adaptive structures for lightweight design [6,7], advanced manufacturing techniques for flexible electronics [8–11], fast response soft robots [12–16], and mechanical metamaterials exhibiting distinct and programmable properties [17–19]. Significant progress has been made in the development of robust analysis and design tools for these functionalised nonlinear structures [5,19–21]. However, experimental techniques for their validation and verification lag behind numerical methods, as experimental procedures to monitor the behaviour of shape-shifting structures and metamaterials require control over the overall shape of the specimens [22,23] and multiple synchronised loading apparatuses [24,25]. This paper aims to bridge the gap in actuation capabilities for shape-shifting metamaterials by introducing a novel experimental test rig. This rig uniquely combines actuation on a global and macroscopic scale with actuation on a local and microscopic one (*i.e.*, embedded actuation) [15].

Experimental methods for structures and materials susceptible to instabilities are mainly based on force- or displacement-controlled loading using a single actuation system. However, important metrics cannot be measured using this approach, especially in the case of unstable buckling events leading to dynamic changes of the structure's shape. An

* Corresponding author at: Exeter Technologies Group (ETG), Department of Engineering, University of Exeter, Exeter EX4 4QF, UK.
*E-mail addresses:* qicheng.zhang@bristol.ac.uk (Q. Zhang), j.shen3@exeter.ac.uk (J. Shen), m.garrad@bristol.ac.uk (M. Garrad), f.scarpa@bristol.ac.uk (F. Scarpa), alberto.pirrera@bristol.ac.uk (A. Pirrera), rainer.groh@bristol.ac.uk (R.M.J. Groh).
[1] Co-first authors. Qicheng Zhang and Jiajia Shen contributed equally to the work.

https://doi.org/10.1016/j.tws.2024.112222
Received 8 May 2024; Received in revised form 25 June 2024; Accepted 10 July 2024
Available online 15 July 2024

example of these metrics are the energy barriers surrounding a stable equilibrium. These quantify how much energy needs to be input into the system to allow the transition to a new equilibrium. Measuring these energy barriers is relevant, for instance, to characterise the sudden buckling of shells, which is governed by the erosion of an energy barrier via small dimple imperfections forming in the shell's wall [26–28]. Thompson and collaborators proposed a bi-axial testing technique, where an independent lateral force is applied to the structure in addition to the primary loading to ascertain the magnitude of the energy barrier of the dimple with increasing axial compression [27,29–32]. In earlier versions of this technique the secondary actuation point, *i.e.* the lateral probing force, could only push and not pull [27]. Neville et al. [22] developed a novel test rig, where probes could both push and pull, to trace nonlinear equilibrium paths beyond limit points, *i.e.* to traverse the otherwise unstable collapse points [23–25]. More recently, non-destructive health monitoring techniques that combine probing with machine learning have been proposed to estimate the in situ load-carrying capacities of structures in service [33].

The methods discussed above focus on probing the energy barrier or other characteristics of the energy landscape of structures prone to buckling, where the loss of stability is seen as a failure mode. Traversing an energy barrier is, however, also important to design functional instabilities — *e.g.* in multi-stable shape-shifting structures — as it defines the amount of energy required to initiate the transition between different stable configurations [21,34]. Consequently, understanding and quantifying such energy barriers experimentally is important for validating simulations of shape-shifting structures as well as during the certification procedures of prototypes.

In recent work [15], we proposed a multi-scale actuation technique to achieve shape-shifting in multi-stable metamaterials. Smaller-scale actuators were embedded within the metamaterial to shift its deformation mode from one stable state to another, with the global strain energy of the metamaterial controlled by a compressive force applied at the global length scale. Importantly, we demonstrated that the embedded actuation technique has superior energy efficiency in shape-shifting, as the lowest energy barrier between the two stable states can be more directly surpassed using the embedded actuators. Hence, this embedded shape-shifting mechanism holds particular promise for scenarios constrained by power availability, such as microrobots employed for medical diagnosis [35,36]. The successful execution of shape-shifting and measurement of the associated traversed energy barriers depends critically on the judicious selection of the embedded actuation parameters, encompassing both the location and direction of applied forces. To validate and verify the effectiveness of local actuation of metamaterials, and to complement robust numerical simulations, high-fidelity experimental test rigs are therefore important.

In this paper, we present the details of a bi-axial test rig for shape-shifting metamaterials that combines actuation at two length scales. The test rig was designed to quantify the energy barrier within a typical multi-stable lattice mechanical metamaterial [15,37]. The paper is organised as follows. Section 2 reviews the mechanics of the multi-stable mechanical metamaterial and defines the scope of the work presented. Section 3 provides details of the test rig with the experimental results presented in Section 4. Concluding remarks are made in Section 5.

## 2. Problem definition

We focus on a lattice mechanical metamaterial consisting of an elastomeric matrix with a 3 by 3 square array of circular holes. The structure is shown in Fig. 1(a). The holes have radius $r$ and center-to-center distance $a$, chosen so that the initial porosity is $\phi_0 = \pi r^2/a^2 = 0.6$. The metamaterial has vertical edges broken up by columns of semi-circles separated by straight segments of height $a - r$. In this study, we adopt the geometry and material properties of the sample as presented in Table 1. Figs. 1(b–d) present the nonlinear equilibrium path of the metamaterial under global axial compression at the top edge. These results are produced by simulations using an in-house nonlinear FE solver [5] (see previous work [15] for details). There are three stable post-buckling modes under global compression: two shearing modes bifurcating from the natural loading path of global compression and one polarised mode on an isolated path (see mode shapes in Fig. 1(b)). Hence, by being compressed from the top the metamaterial naturally buckles into one of the two mirror-symmetric sheared modes, shearing either to the left or to the right. Stable deformation in the polarised mode is also possible, but the metamaterial needs to be nudged towards left–right symmetry to overcome the energy barrier separating the polarised mode from the sheared modes.

The preferential deformation sequence under globally applied compression can be changed using a technique known as *modal nudging* [38], inducing a natural tendency towards the polarised mode upon compression. Modal nudging introduces geometric perturbations that are affine to a desired post-buckling deformation mode, thereby effectively reprogramming the structure's natural loading path. In the present study, we introduce a scaled deformation profile of the polarised mode into the baseline geometry. Consequently, the metamaterial seamlessly deforms into the polarised mode upon global compression, thereby positioning the shear modes on isolated equilibrium paths. Our previous work has shown that, in this arrangement, it is easier to transition reliably between the sheared and polarised modes using embedded actuators that apply forces onto the central hole of the metamaterial, as shown in Fig. 1(e). This approach surpasses the conventional method of relying on global actuation, which induces shape-shifting through pre-buckling to post-buckling state deformations.

Our previous work [15] demonstrated that a pair of concentrated forces (in $y$-direction) applied to the central hole efficiently achieves mode switching between the polarised mode and the shear mode as long as the metamaterial is sufficiently pre-compressed via globally applied compression. Fig. 1(e), schematically shows this mode switch and the corresponding central force, $F_n$, *vs* displacement, $u_n$, relationship. By applying actuation when in the polarised mode via the embedded forcing, the pre-compressed metamaterial loses stability at a maximum limit point, dynamically snaps into one shear mode, and stabilises therein once the embedded forcing is removed ($F_n = 0$ at ES1 in Fig. 1(e)). The area enclosed by the $F_n$–$u_n$ curve up to the force limit point represents the energy barrier between the polarised mode and the shear mode.

Here, our goal is to present a test rig that enables experimental measurement of the energy barrier between polarised and shear modes within the multi-stable lattice metamaterial. The measurement strategy relies on measuring both the force and displacement along the embedded actuation pathway, culminating at the force limit point where snap-through into the second mode occurs. To ensure accurate energy barrier determination, the pair of embedded forces must maintain a strictly $Y$-direction throughout the actuation process. However, the metamaterial's shape-shifting behaviour from the polarised to the sheared mode is intrinsically accompanied by symmetry breaking, which presents a difficult challenge: designing an actuation system that permits unconstrained movement of the actuation points in the $X$-direction while simultaneously enforcing exclusive force application in the $Y$-direction. Smooth linear bearings, wedge loading structures, and miniature load cells enable this capability. This design offers potential for developing complex loading systems suitable for nonlinear structural testing where shape-shifting triggered by follower actuation inputs is required. The key advantage lies in its ability to accommodate changing load directions and positions without introducing extraneous constraints.

## 3. Experimental setup, procedure and verification

### 3.1. Test rig and experimental setup

The CAD model of the test rig is shown in Fig. 2. The schematic of the test rig consists of individually labelled and numbered parts,

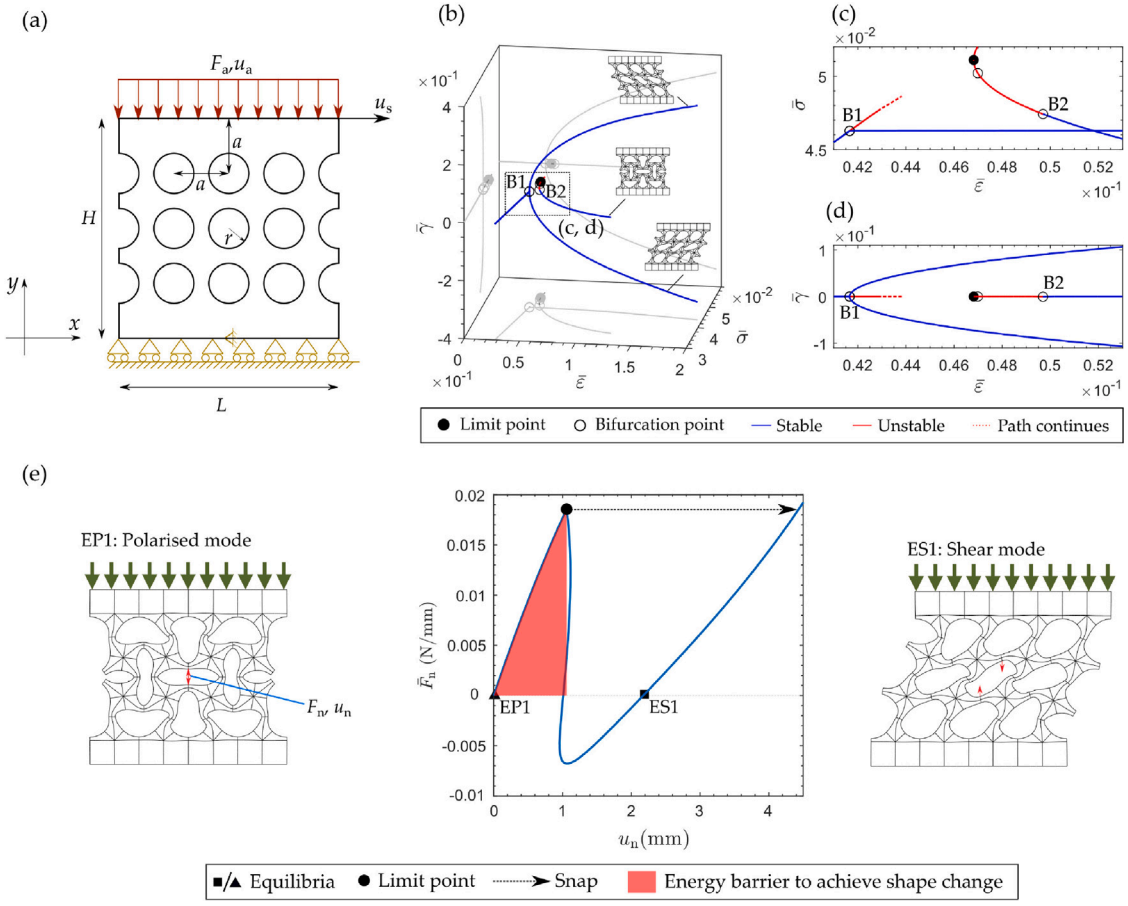


**Fig. 1.** (a) Geometry of the lattice mechanical metamaterial and the applied boundary conditions. Global axial compression $u_a$ is applied on the top edge with the reaction force being $F_a$. The bottom edge is constrained. The top edge is free to move horizontally with shear displacement $u_s$. (b–d) Equilibrium paths of the perfect lattice metamaterial under pure compression. There are two stable shearing modes on the natural loading path and one stable polarised mode on an isolated path. $\bar{\varepsilon}$, $\bar{\sigma}$, and $\bar{\gamma}$ are the normalised axial compression displacement, axial force and shear displacement, respectively. Circles B1 and B2 represent bifurcation points on the fundamental path and isolated path, respectively. (e) A pair of vertical forces applied in the central hole triggers mode switching between the stable polarised mode (EP1) and one stable sheared mode (EP2). The direction of the actuation forces remains vertical throughout the actuation and the actuation points are free to move horizontally. The actuation force $F_n$–displacement $u_n$ relationship during the mode switch is plotted.
*Source:* The figures are reproduced from the authors' previous work [15].

**Table 1**
The material and geometric properties of the considered metamaterial. The definition of the geometric parameters refers to Fig. 1(a). The geometric properties are the same as those considered by Medina et al. [37].

| Shear modulus $\mu$ (kPa) | Poisson's ratio $\nu$ | Length $L$ (mm) | Height $H$ (mm) | Center to center distance $a$ (mm) | Radius of holes $r$ (mm) | Depth $D$ (mm) |
|---|---|---|---|---|---|---|
| 49 | 0.48 | 50.2 | 50.2 | 12.55 | 5.46 | 40 |

details of which are given below. The rig has two independent actuation inputs: (1) global actuation at the top edge to compress the metamaterial into the post-buckling regime (see Fig. 2(c)); and (2) embedded actuation applied via two steel bars inserted in pre-cast circular holes of 1.5 mm diameter adjacent to the central hole of the metamaterial (see Fig. 2(d)), enabling mode switching from the polarised mode to one of the shear modes.

Global compression is applied by movement of two support structures, which are adjustable through manual linear stages (Edmund Optics, resolution 0.1 mm), as shown in Fig. 2(c). Compression support 1 is connected to loading plate 1 via load cell 5 (DYMH-103-50 kg), to measure the global compression force. Compression support 2 is connected to loading plate 2 through a low friction linear ball bearing (IKO BSP-20-45SL), enabling shear displacement at the top edge without lateral constraints.

The embedded actuation force is applied through steel bars (in $Z$-direction) connected to a structure comprising wedges and frames. These supports rest on six low friction linear ball bearings, as shown in Fig. 2(d). This setup ensures that a pair of equal and opposite forces in $Y$-direction is applied at the extremities of each of the steel bars connected to the frames, with the bars remaining free to move in the $X$-direction. This approach reproduces the actuation forces that achieves shape-shifting in an accompanying numerical study [15]. Both ends of both steel bars, which are themselves inserted into the small holes in the metamaterial, are connected to load cells (Forsentek FMZJ-1 kg). An additional four load cells are fixed to the frames. The two frames are connected to the wedges using linear bearings (IKO BSR-20-80SL), allowing the frames' movement along the $Y$-direction (see the red arrows in Fig. 2(f)) to be adjusted by the wedges while moving freely along the $X$-direction. The moving wedges are combined with the wedge supports using linear bearings (IKO BSP-20-45SL). The $Y$-position of wedge support 1 can be adjusted by a linear stage. The wedge has a 90° angle, forcing the displacement of frames 1 and 2 along the $Y$-direction to be the same but in opposite directions, equal to the displacement of wedge support 2 along the $X$-direction.

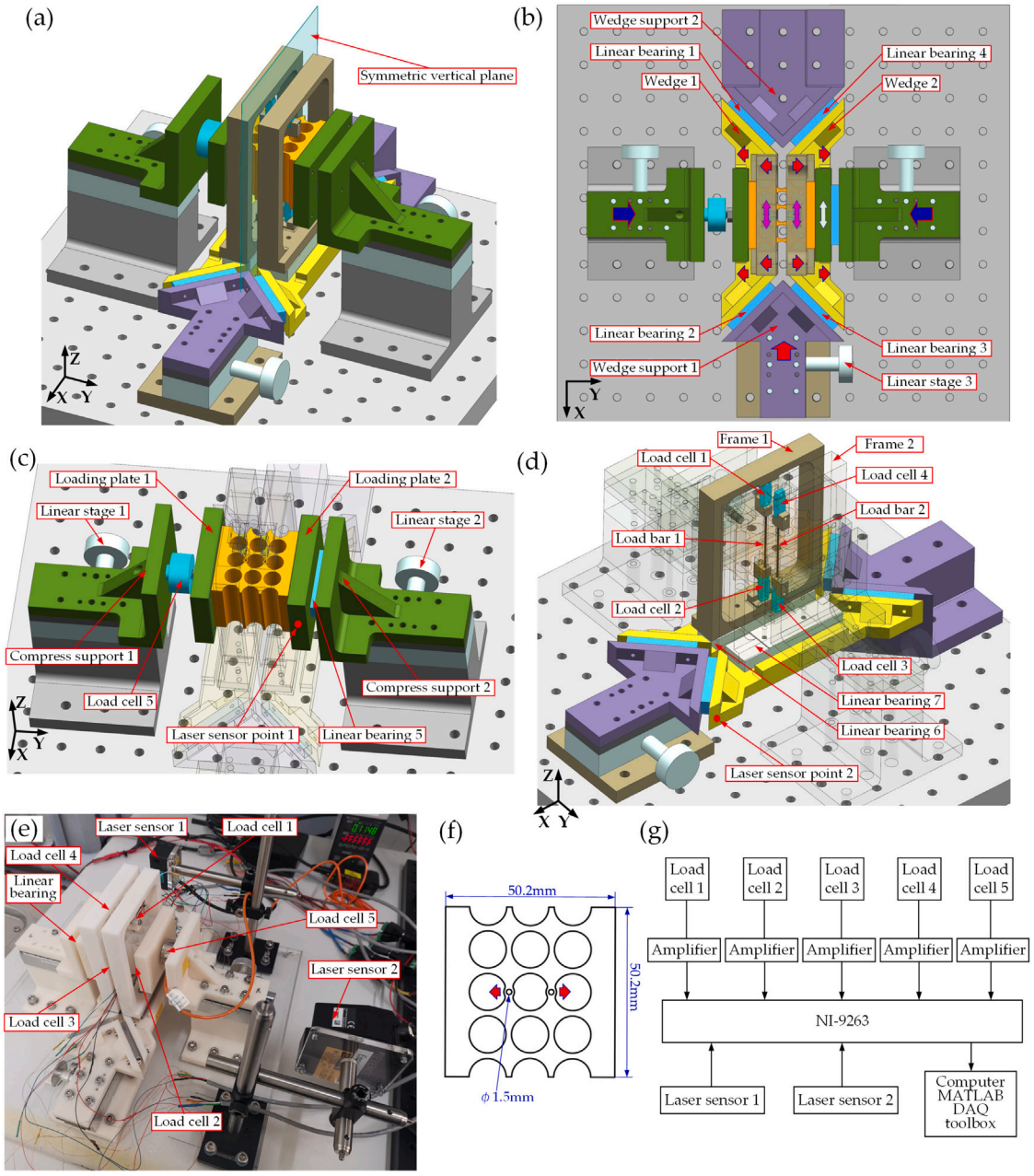


**Fig. 2.** Experimental setup. (a) The 3D and (b) planar view of the CAD model of the whole test rig. (c) Global compression loading parts of the rig. (d) Embedded actuation loading parts of the rig. (e) Photo of the actual test rig. Two laser sensors are used to record the displacements along X and Y directions of the embedded forcing point. (f) CAD model of the sample. A pair of circular holes with a diameter of 1.5 mm is introduced next to the central hole. Steel bars are inserted into these holes to apply the embedded forcing. The red arrows indicate the direction of the applied force. (g) Schematic overview of the sensor and data logging system, demonstrating the flow of information from sensors to data acquisition software.

Laser sensor 1 (OMRON ZX2-LD100L, resolution 5 μm) measures the $Y$-displacement of loading plate 2, while laser sensor 2 (KEYENCE LK-G152, resolution 0.5 μm) measures the $X$-displacement of the moving wedge in the embedded actuation test. The NI-9263 module (National Instruments) connects to a PC for data recording through the MATLAB DAQ toolbox. Five load cells are connected to amplifiers (SMOWO RW-ST01 A) and the data recording module, along with the two laser sensors (Fig. 2(g)).

### 3.2. Test sample fabrication

The metamaterial sample for testing was fabricated using a drop-casting process. First, moulds were additively manufactured using a Stratasys Objet Connex-J826 3D printer, using Verowhite resin. The CAD model for the mould was generated by integrating a scaled deformation profile of the polarised mode into the geometry. The magnitude of the polarised seed needs to be large enough to ensure that the first buckling mode of the metamaterial is the polarised rather than the sheared mode. The sample size matches the dimensions specified in Table 1. Notably, the depth of the sample $D$ was set to 40 mm to prevent out-of-plane buckling during testing. Following printing, the moulds were washed with sodium hydroxide and dried thoroughly.

Dragon Skin 10 NV elastomer was mixed according to the manufacturer's instructions, degassed and then poured into the moulds. The elastomer was cured for 2 h at room temperature. More details of the fabrication process can be found in Section 6 of the Supplementary Materials in the authors' previous work [15].

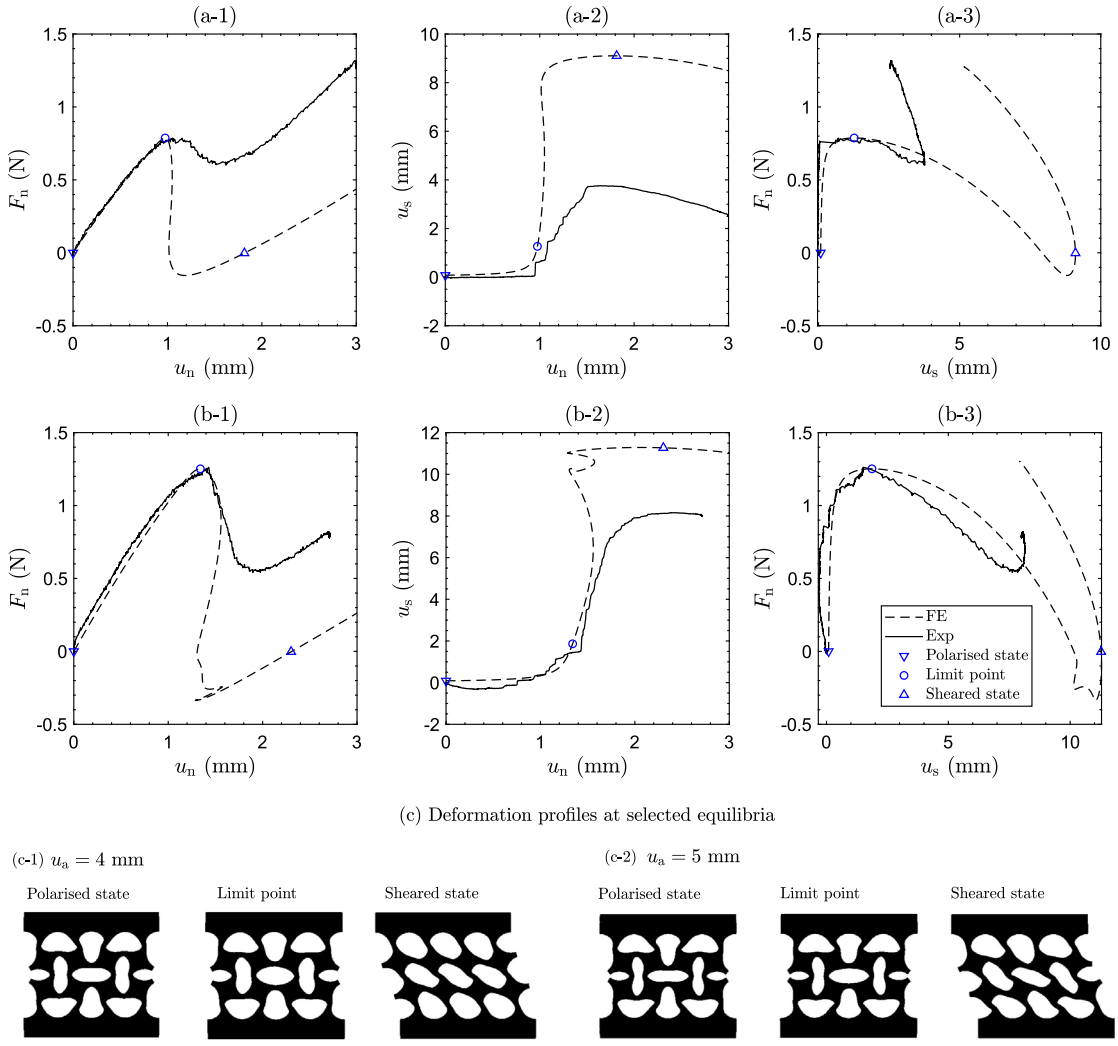


**Fig. 3.** Comparison of the active nudging equilibrium paths from experimental testing and nonlinear FE simulations for global pre-compression of (a) 4 mm and (b) 5 mm, respectively. (c) The deformation profiles of the test sample at key states from FE simulations. Note that the sample dimensions are presented in Table 1.

### 3.3. Experimental procedure

The procedure followed during the experimental testing is as follows:

- **Establish the Symmetric Plane** ($X$-$Z$ **plane**). Before installing the sample into the test rig, a plate (in $X$-$Z$ plane) is clamped by the wedge and the compression supports in the middle of the rig. This allows the establishment of a symmetric plane (Fig. 2(a)) of movement for the wedge and compression supports. This action also provides a symmetry reference plane for all following test procedures and ensures that deformation symmetry is preserved.
- **Initial Symmetric Pre-compression.** Compression supports 1 and 2 are adjusted by the same value but in opposite directions to maintain the system's symmetry plane. Once the sample is installed, symmetrical pre-compression is applied by adjusting compression supports 1 and 2 to gradually put the mounted metamaterial sample into a polarised mode, as shown in Fig. 2(c). Two pre-compression levels, $u_a = 4$ mm and 5 mm, have been used in the test.
- **Maintaining Force Equilibrium.** While applying the pre-compression, the $Y$-position of wedge support 1 is manually fine-tuned to maintain the force of the load cells 1–4 close to the initial value in the free state. Due to the sample's weight, the initial force of the load cells 1–4 is not zero (<0.5 N), even without compression applied. This initial force is later offset in data post-processing.
- **Embedded Actuation Test.** After achieving the desired pre-compression displacement, the embedded actuation test is performed by manually adjusting the linear stage 3 at a constant loading rate (around 5 mm/min). The mode shape transforms from the polarised mode into the shear mode, and signals from the five load cells and two laser sensors are recorded simultaneously.

### 3.4. FE model for verification

To verify the experimental setup, we have developed a three-dimensional nonlinear finite element (FE) model within the commercial FE package Abaqus CAE. The geometry of the FE model is based on the CAD model for the sample fabrication and is discretised using 8-node linear brick, reduced integration elements with hourglass control, C3D8R in Abaqus CAE. Abaqus CAE native mesh generator was adopted to produce a structured uniform mesh. A mesh sensitivity study was conducted to determine a mesh size balancing accuracy and computational effort. The finite element mesh utilises a structured non-uniform element size with hexahedral (hex) elements. The hollow region employs an element size of 0.265 mm, while the top edge region uses a larger element size of 0.523 mm. Uniform elements

of 0.8 mm are used in the longitudinal direction. For simplicity, to approximate the embedded actuation forces, the FE model uses a pair of concentrated loads with opposite directions applied to the central hole.

A multi-step analysis procedure was adopted to trace the nonlinear response of the pre-compressed metamaterial upon application of the embedded actuation force. The initial step uses the General Static solver to simulate the displacement-controlled global loading required to establish the desired pre-compression. This is followed by the embedded forcing step, which employs the Riks arc-length solver [39] to effectively navigate the complex snap-through phenomenon. Geometric nonlinearities are intrinsically accounted for throughout both analysis phases to ensure a comprehensive representation of the structural behaviour. Further details of the analysis procedure can be found in the authors' previous work [15].

## 4. Results

Fig. 3 presents the results obtained from the test rig for two different pre-compression levels with $u_a = 4$ mm and 5 mm, respectively. The embedded actuation process starts from the polarised mode, characterised by a shear displacement of zero. To facilitate a comparative analysis, the results from the nonlinear finite element simulation are presented alongside the experimental data. Excellent correlation is observed between experiments and simulations, with a high degree of agreement persisting up to the critical forcing limit point. As expected, beyond this juncture, a notable increase in shear displacement is evident. From Fig. 3(a-2) and (b-2), we can confidently assert that the test rig exhibits a robust capability to capture the snap-through point, underscoring its effectiveness in characterising the shape-shifting transition.

With further loading beyond the limit point, the shear displacement increases and a notable divergence emerges between the finite element simulation and the experimental results. Crucially, neither of the two experiments attains a stable shear mode characterised by $F_n = 0$ N. This discrepancy likely stems from several factors.

First, frictional effects within the glide mechanism likely play an important role. While idealised as perfectly smooth in the FE model, the experimental setup inevitably encounters frictional resistance. Notably, the current configuration employs a single glide at the framework's base, potentially introducing a moment upon loading and further exacerbating frictional effects. Secondly, the viscoelastic nature of the rubber material warrants consideration. As Brinkmeyer et al. [40] have demonstrated, viscoelasticity (not accounted for herein) can profoundly influence the multi-stability of elastomeric structures and affect the effective stiffness, thereby changing the observed equilibria. Thirdly, a discrepancy exists between the idealised point load employed in the FE model and the experimental setup that uses two rods of finite radius. This distinction becomes particularly significant within the advanced post-buckling regime, where material softness can lead to substantial local deformation around the load application point.

Interestingly, the experimental results for pre-compression level $u_a = 5$ mm exhibit better agreement with the simulations compared to the case with $u_a = 4$ mm. This improved correlation likely arises from the increased energy release associated with the snap-through event when overcoming static friction forces. The additional released energy potentially compensates for frictional losses within the system, leading to a closer approximation of the idealised frictionless scenario modelled in the finite element simulation. To solidify this reasoning, however, a more comprehensive experimental dataset including additional pre-compression levels is necessary. This investigation will be the focus of future studies.

Since the test rig can accurately capture the force limit point, we can calculate the energy barrier for mode shifting based on the measured nonlinear equilibrium path. Specifically, for force-controlled loading, the energy barrier is represented by the area enclosed within the $F_n$-$u_n$ curve before the force limit point, as illustrated by the highlighted shaded area in the equilibrium path in Fig. 4. This can be efficiently calculated using the `trapz` function in MATLAB. Table 2 presents the energy barrier between the polarised and the sheared modes for two pre-compression levels. This energy barrier corresponds to a force-controlled loading scenario. The comparison with the energy barrier computed by finite element analysis shows that experiments and numerics differ by approximately 10%, which is to be expected given the challenges of engineering a precise test rig, the nonlinearity of the phenomena tested (sensitivity to initial conditions) and uncertainties regarding the elastomer's material model. Overall, this comparison demonstrates the capability of the test rig in accurately measuring the nonlinear energy barrier.

**Table 2**
Comparison of the energy barrier between the polarised and the sheared modes from the experimental test and nonlinear FE simulations for two characteristic global pre-compression levels. Also shown are two characteristic indices on the active nudging path, *i.e.* the initial slope $k_{ini}$ and peak load $F_{max}$. Note that the sample dimensions are presented in Table 1. The energy barrier is computed based on the shaded areas of the nonlinear equilibrium paths shown in Fig. 3 using the `trapz` function in MATLAB.

| Global compression | Energy barrier (N · mm) | | $E_{Exp}/E_{FE}$ |
|---|---|---|---|
| $u_a$ (mm) | $E_{FE}$ | $E_{Exp}$ | |
| 4 | 0.417 | 0.476 | 1.143 |
| 5 | 0.927 | 1.002 | 1.081 |

Under displacement-controlled loading, the corresponding energy barrier is the area enclosed up to the displacement limit point. Identifying the displacement limit point experimentally can be challenging. To address this limitation and accurately quantify the displacement-controlled energy barrier, future work will explore the implementation of experimental continuation techniques like those proposed in authors' previous work [23,25].

## 5. Concluding remarks

This paper demonstrates an implementation of a bi-axial loading test rig for exploring the functionalities of nonlinear mechanical metamaterials. Whereas previous work [27,29] primarily focused on thin shells and the loss of stability as a failure mode, our emphasis lies in characterising the energy barrier between distinct stable post-buckling modes that are used for shape-shifting applications in metamaterials as well as generalised shape-shifting structures. Although frictional and other real-world complexities limit the test rig's fidelity in the advanced post-buckling regime, the remarkable correlation between the experimental and FE results prior to the snap-through point proves sufficient for accurately estimating the energy barrier and thereby characterising the energy input required to transition between two distinct states. The capabilities of the test rig are noteworthy as loading and data acquisition from two sets of loading inputs — a global compression and a locally embedded forcing — need to be combined.

While the test rig was specifically designed to measure the energy barrier of a particular type of mechanical metamaterial, the underlying design philosophy holds significant promise for overcoming the challenges associated with experimental characterisation of nonlinear structures/materials. The key concept lies in the 'shape control' [22,25]. Here, it is the local actuator design, which employs a pair of opposing forces with equal magnitude. This approach can be readily adapted to characterise other embedded actuators commonly used in soft robotics, such as pneumatic bellow actuators [41]. On the other hand, the multi-axial nature of the test rig opens doors for a more comprehensive understanding of mechanical metamaterial performance. Traditional testing methods often focus on uniaxial loading [37,42], which does not fully capture the complexities of real-world scenarios. This test rig's ability to apply bi-axial loading provides a more realistic

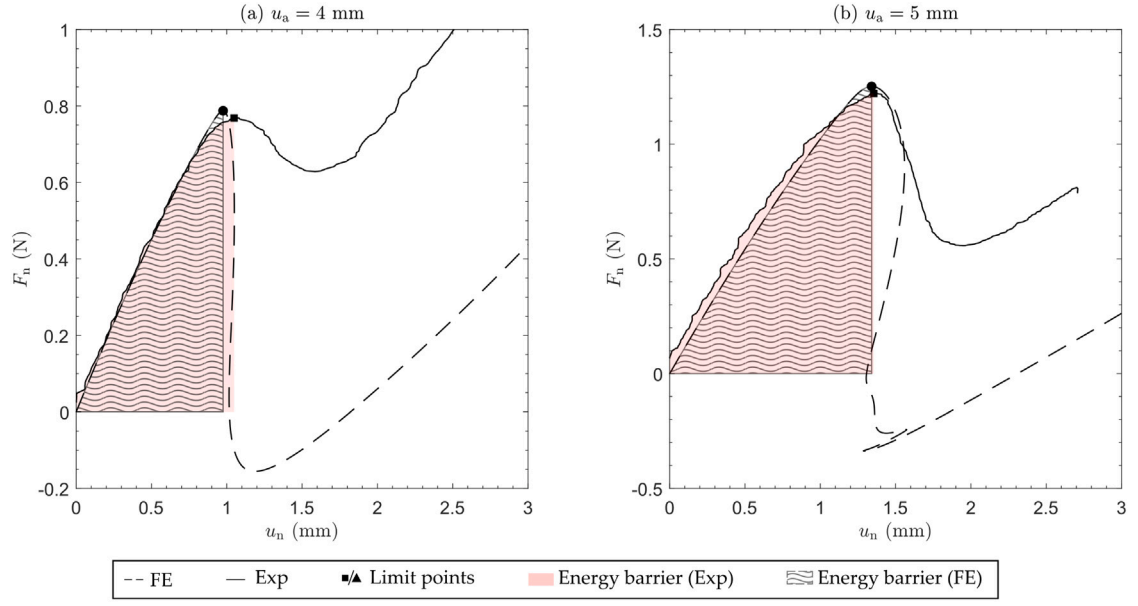


**Fig. 4.** Illustration of the energy barrier between the polarised and sheared modes for global pre-compression of (a) 4 mm and (b) 5 mm, respectively. Compared with Fig. 3, random noise in the experimental data is filtered using the `Smoothdata` function in MATLAB, while maintaining the key features of the equilibrium path. Note that the sample dimensions are presented in Table 1.

representation of the forces a metamaterial might encounter in practice, such as measuring the shear properties of the metamaterial under different axial pre-compression loading. This capability can be invaluable for researchers and engineers developing and optimising metamaterials for specific applications.

Because the current setup relies on a manual gear rotation for both global and embedded loading, this approach presents limitations in terms of smoothness, precision, and control. Moving forward, integrating electric motors and control systems into the test rig presents a promising avenue for overcoming these limitations. Such automation would enable precise actuation profiles with minimal manual intervention, facilitating more consistent and reproducible loading processes. This enhanced controllability and automation would prove particularly valuable for exploring intricate post-buckling behaviours and dynamic shape-shifting phenomena in future studies.

Although the current test rig primarily serves for verification and validation purposes, its potential to become a useful exploration tool for identifying optimal nudging force locations holds considerable promise. Numerical techniques have already demonstrated remarkable progress in charting minimum energy paths and corresponding actuation strategies for efficient mode switching [21,34,43]. Translating these capabilities into the experimental realm through the development of robust experimental path-following techniques would unlock a profound understanding of the least-energy paths in physical systems. This knowledge would directly translate into the development of highly efficient shape-shifting structures that exploit multi-stability, marking a significant breakthrough in structural design and control.

## CRediT authorship contribution statement

**Qicheng Zhang:** Writing – original draft (experimental part), Visualization, Validation, Methodology, Investigation, Data curation, Conceptualization. **Jiajia Shen:** Writing – original draft, review & editing, Visualization, Validation, Software, Project administration, Methodology, Investigation, Formal analysis, Data curation, Conceptualization. **Martin Garrad:** Resources, Methodology, Conceptualization. **Fabrizio Scarpa:** Writing – review & editing, Supervision, Funding acquisition. **Alberto Pirrera:** Writing – review & editing, Supervision, Resources, Project administration, Conceptualization. **Rainer M.J. Groh:** Writing – review & editing, Supervision, Software, Resources, Project administration, Methodology, Funding acquisition, Conceptualization.

## Declaration of competing interest

The authors declare that they have no known competing financial interests or personal relationships that could have appeared to influence the work reported in this paper.

## Data availability

Data are available at the University of Bristol data repository, data.bris, at https://data.bris.ac.uk/data/dataset/1n7g692ynrlht214cxm7yk77qi.

## Acknowledgements

J.S. was funded by the Leverhulme Trust, United Kingdom through a Philip Leverhulme Prize awarded to R.M.J.G. R.M.J.G. was funded by the Royal Academy of Engineering, United Kingdom under the Research Fellowship scheme [RF\201718\17178]. J.S. was also funded by a Research Fellowship from Exeter Technologies Group at the University of Exeter. Q.Z. acknowledges the support of the IMPACT fellowship from Swansea University. F.S. also acknowledges the support of the ERC-2020-AdG 101020715 NEUROMETA project.

## Appendix. Axial compression test results

To verify the functionality of the test rig, we initiated the experimental campaign with a series of axial compression tests. The test sample was designed with geometric perturbations that aligned with the stable polarised mode, ensuring its emergence as the natural loading path under axial compression. To obtain the stable shear mode, we implemented a multi-stage procedure. First, the sample was loaded into the advanced post-buckling regime along its natural loading path corresponding to the polarised mode. Subsequently, we applied a manual force at the top edge of the metamaterial to guide the structure to stabilise in the shear mode. Finally, we gradually unloaded the sample to obtain the stable segment of the isolated equilibrium path corresponding to the shear mode. With decreasing axial compression, the sample exhibited a predictable snap-back behaviour towards the natural loading path upon encountering a limit point instability. The axial displacement $u_a$ at loading plate 1 and the shear displacement $u_s$

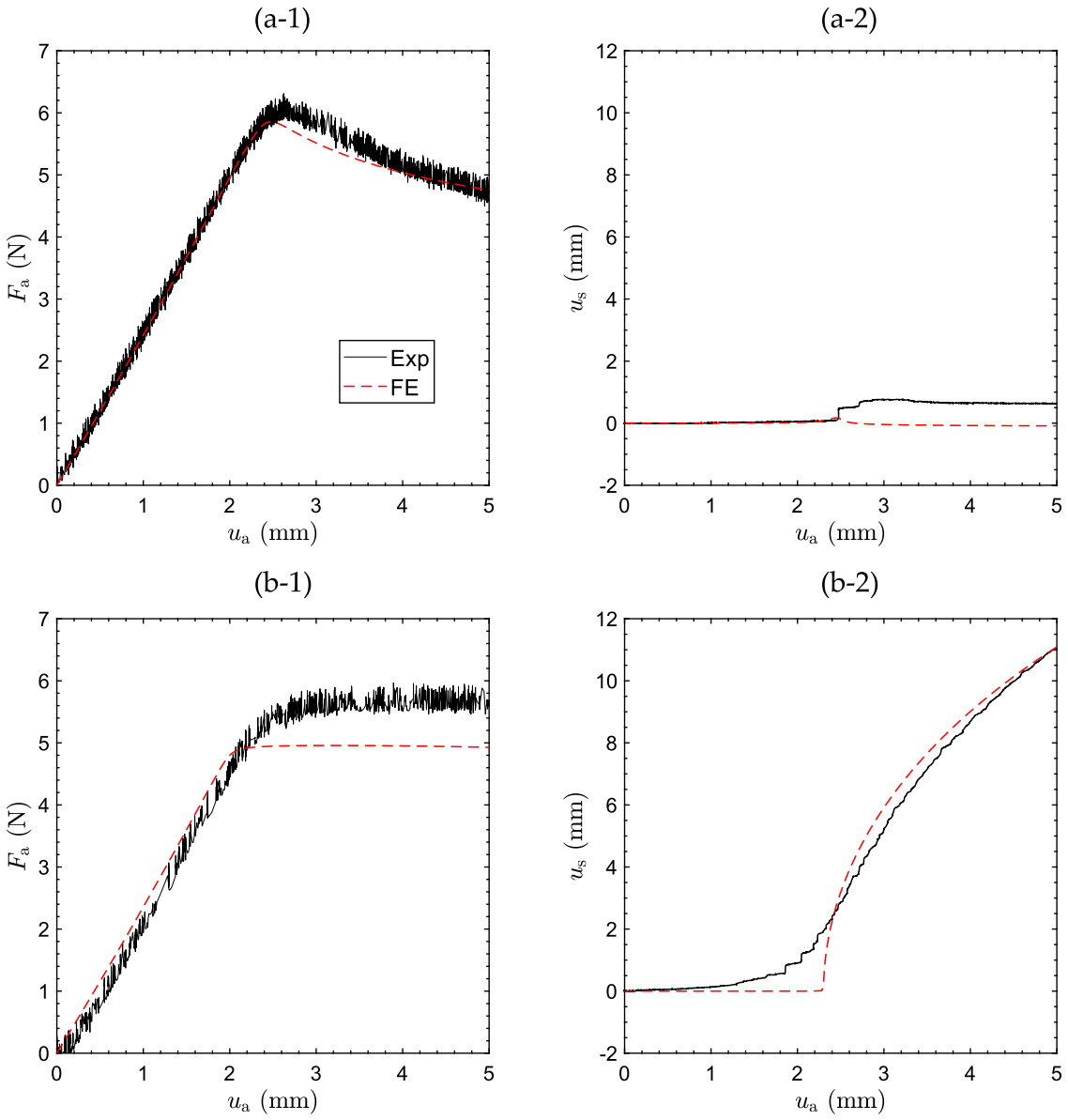


**Fig. A.1.** Response of the experimental samples with polarised geometric perturbation. (a) Natural loading path corresponding to the polarised mode. (b) Isolated path corresponding to the shear mode. Note that the size and the material properties of the sample are presented in Table 1.

at loading plate 2 (without horizontal constraint), as shown in Fig. 2(e) are measured separately using two laser sensors. These results are presented in Fig. A.1 and generally show good correlation with the FE simulation, thereby verifying the effectiveness of the test rig.

## References


[1] Z.P. Bažant, Structural stability, Int. J. Solids Struct. 37 (1–2) (2000) 55–67.

[2] N.S. Trahair, M. Bradford, D. Nethercot, L. Gardner, The Behaviour and Design of Steel Structures to EC3, CRC Press, 2017.

[3] J. Shen, M.A. Wadee, Length effects on interactive buckling in thin-walled rectangular hollow section struts, Thin-Walled Struct. 128 (2018) 152–170.

[4] P.M. Reis, A perspective on the revival of structural (in) stability with novel opportunities for function: from buckliphobia to buckliphilia, J. Appl. Mech. 82 (11) (2015) 111001.

[5] R.M.J. Groh, D. Avitabile, A. Pirrera, Generalised path-following for well-behaved nonlinear structures, Comput. Methods Appl. Mech. Engrg. 331 (2018) 394–426.

[6] G. Arena, R.M.J. Groh, A. Brinkmeyer, R. Theunissen, P. M. Weaver, A. Pirrera, Adaptive compliant structures for flow regulation, Proc. R. Soc. A 473 (2204) (2017) 20170334.

[7] E. Wheatcroft, J. Shen, R.M.J. Groh, A. Pirrera, M. Schenk, Structural function from sequential, interacting elastic instabilities, Proc. R. Soc. A 479 (2272) (2023) 20220861.

[8] B. Li, Y.-P. Cao, X.-Q. Feng, H. Gao, Mechanics of morphological instabilities and surface wrinkling in soft materials: a review, Soft Matter 8 (21) (2012) 5728–5745.

[9] C.-M. Chen, S. Yang, Wrinkling instabilities in polymer films and their applications, Polym. Int. 61 (7) (2012) 1041–1047.

[10] J. Shen, A. Pirrera, R.M.J. Groh, Building blocks that govern spontaneous and programmed pattern formation in pre-compressed bilayers, Proc. R. Soc. A 478 (2265) (2022) 20220173.

[11] T. Jin, X. Cheng, S. Xu, Y. Lai, Y. Zhang, Deep learning aided inverse design of the buckling-guided assembly for 3D frame structures, J. Mech. Phys. Solids 179 (2023) 105398.

[12] Y. Tang, Y. Chi, J. Sun, T.-H. Huang, O.H. Maghsoudi, A. Spence, J. Zhao, H. Su, J. Yin, Leveraging elastic instabilities for amplified performance: Spine-inspired high-speed and high-force soft robots, Sci. Adv. 6 (19) (2020) eaaz6912.

[13] A. Pal, V. Restrepo, D. Goswami, R.V. Martinez, Exploiting mechanical instabilities in soft robotics: control, sensing, and actuation, Adv. Mater. 33 (19) (2021) 2006939.

[14] Y. Chi, Y. Li, Y. Zhao, Y. Hong, Y. Tang, J. Yin, Bistable and multistable actuators for soft robots: Structures, materials, and functionalities, Adv. Mater. 34 (19) (2022) 2110384.

[15] J. Shen, M. Garrad, Q. Zhang, O. Leao, A. Pirrera, R.M.J. Groh, Active reconfiguration of multistable metamaterials for linear locomotion, Phys. Rev. B 107 (21) (2023) 214103.
[16] J. Shen, M. Garrad, Q. Zhang, V. Wong, A. Pirrera, R.M.J. Groh, A rapid-response soft end effector inspired by the hummingbird beak, J. R. Soc. Interface (2024) (Accepted).
[17] K. Bertoldi, V. Vitelli, J. Christensen, M. Van Hecke, Flexible mechanical metamaterials, Nat. Rev. Mater. 2 (11) (2017) 1–11.
[18] J. Bunyan, S. Tawfick, Exploiting structural instability to design architected materials having essentially nonlinear stiffness, Adv. Eng. Mater. 21 (2) (2019) 1800791.
[19] B. Deng, A. Zareei, X. Ding, J.C. Weaver, C.H. Rycroft, K. Bertoldi, Inverse design of mechanical metamaterials with target nonlinear response via a neural accelerated evolution strategy, Adv. Mater. 34 (41) (2022) 2270287.
[20] C.S. Ha, D. Yao, Z. Xu, C. Liu, H. Liu, D. Elkins, M. Kile, V. Deshpande, Z. Kong, M. Bauchy, et al., Rapid inverse design of metamaterials based on prescribed mechanical behavior through machine learning, Nature Commun. 14 (1) (2023) 5765.
[21] G. Wan, S.J. Avis, Z. Wang, X. Wang, H. Kusumaatmaja, T. Zhang, Finding transition state and minimum energy path of bistable elastic continua through energy landscape explorations, J. Mech. Phys. Solids 183 (2024) 105503.
[22] R.M. Neville, R.M.J. Groh, A. Pirrera, M. Schenk, Shape control for experimental continuation, Phys. Rev. Lett. 120 (25) (2018) 254101.
[23] R.M. Neville, R.M.J. Groh, A. Pirrera, M. Schenk, Beyond the fold: experimentally traversing limit points in nonlinear structures, Proc. R. Soc. A 476 (2233) (2020) 20190576.
[24] J. Shen, R.M.J. Groh, M. Schenk, A. Pirrera, Experimental path-following of equilibria using Newton's method. Part I: Theory, modelling, experiments, Int. J. Solids Struct. 210 (2021) 203–223.
[25] J. Shen, R.M.J. Groh, M. Schenk, A. Pirrera, Experimental path-following of equilibria using newton's method. part II: Applications and outlook, Int. J. Solids Struct. 213 (2021) 25–40.
[26] J. Horák, G.J. Lord, M.A. Peletier, Cylinder buckling: The mountain pass as an organizing center, SIAM J. Appl. Math. 66 (5) (2006) 1793–1824.
[27] E. Virot, T. Kreilos, T.M. Schneider, S.M. Rubinstein, Stability landscape of shell buckling, Phys. Rev. Lett. 119 (22) (2017) 224101.
[28] R.M.J. Groh, A. Pirrera, On the role of localizations in buckling of axially compressed cylinders, Proc. R. Soc. A 475 (2019) 20190006.
[29] J.M. Thompson, Advances in shell buckling: theory and experiments, Int. J. Bifurc. Chaos Appl. Sci. Eng. 25 (01) (2015) 1530001.
[30] J.W. Hutchinson, J.M.T. Thompson, Nonlinear buckling interaction for spherical shells subject to pressure and probing forces, J. Appl. Mech. 84 (6) (2017).
[31] K.K. Yadav, N.L. Cuccia, E. Virot, S.M. Rubinstein, S. Gerasimidis, A nondestructive technique for the evaluation of thin cylindrical shells' axial buckling capacity, J. Appl. Mech. 88 (5) (2021) 051003.
[32] S. Ankalhope, S. Jose, Non-destructive prediction of buckling load of axially compressed cylindrical shells using least resistance path to probing, Thin-Walled Struct. 170 (2022) 108497.
[33] J. Shen, L. Lapira, M.A. Wadee, L. Gardner, A. Pirrera, R.M.J. Groh, Probing in situ capacities of prestressed stayed columns: towards a novel structural health monitoring technique, Phil. Trans. R. Soc. A 381 (2244) (2023) 20220033.
[34] K. Song, F. Scarpa, M. Schenk, Identifying the energy threshold for multistable tensegrity structures using a Mountain Pass algorithm, Int. J. Solids Struct. 283 (2023) 112472.
[35] B. Guo, Y. Liu, R. Birler, S. Prasad, Self-propelled capsule endoscopy for small-bowel examination: proof-of-concept and model verification, Int. J. Mech. Sci. 174 (2020) 105506.
[36] Y. Zhang, J. Shen, Y. Yan, J. Tong, L. Zhang, Y. Liu, Enhancing the mobility of small-scale robots via nonlinear structural springs exhibiting negative stiffness, J. Appl. Mech. 91 (8) (2024).
[37] E. Medina, P.E. Farrell, K. Bertoldi, C.H. Rycroft, Navigating the landscape of nonlinear mechanical metamaterials for advanced programmability, Phys. Rev. B 101 (6) (2020) 064101.
[38] B.S. Cox, R.M.J. Groh, D. Avitabile, A. Pirrera, Modal nudging in nonlinear elasticity: Tailoring the elastic post-buckling behaviour of engineering structures, J. Mech. Phys. Solids 116 (2018) 135–149.
[39] E. Riks, An incremental approach to the solution of snapping and buckling problems, Int. J. Solids Struct. 15 (7) (1979) 529–551.
[40] A. Brinkmeyer, M. Santer, A. Pirrera, P. Weaver, Pseudo-bistable self-actuated domes for morphing applications, Int. J. Solids Struct. 49 (9) (2012) 1077–1087.
[41] N. El-Atab, R.B. Mishra, F. Al-Modaf, L. Joharji, A.A. Alsharif, H. Alamoudi, M. Diaz, N. Qaiser, M.M. Hussain, Soft actuators for soft robotic applications: a review, Adv. Intell. Syst. 2 (10) (2020) 2000128.
[42] X. Ren, J. Shen, A. Ghaedizadeh, H. Tian, Y.M. Xie, Experiments and parametric studies on 3D metallic auxetic metamaterials with tuneable mechanical properties, Smart Mater. Struct. 24 (9) (2015) 095016.
[43] R. Sachse, M. Bischoff, A variational formulation for motion design of adaptive compliant structures, Internat. J. Numer. Methods Engrg. 122 (4) (2021) 972–1000.